CHAPTER 5

Above-Ordering-Temperature Anomalous Hall Effect in A Rare Earth Doped Topological Insulator $BiSbTe_3$

5.1 Introduction

The anomalous Hall effect (AHE) is a fundamental transport property of magnetic materials in which the interaction of magnetism and spin-orbit coupling creates a transverse Hall voltage perpendicular to the applied current and the magnetization [250]. The microscopic mechanisms of AHE are classified into two categories: intrinsic mechanisms related to Berry curvature and extrinsic mechanisms involving asymmetric scattering. The intrinsic AHE is controlled by a material's electronic structure, which causes an electron to gain transverse momentum as it travels between scattering events [251]–[253]. The extrinsic AHEs on the other hand, rely on scattering off of electrons causes by various defects and impurities in the periodic potential of crystals[70], [71], [254]. Because of its widespread use in magnetic sensors, random access memory, and spin logic devices, AHE is regaining popularity in condensed matter physics.

The intrinsic mechanism is connected to the Berry curvature of electronic bands, which results from spin-orbit interaction. More recently, it was pointed out that the scalar spin chirality (SSC) $S_i \cdot (S_j \times S_k)$ also contributes to the AHE as a part of intrinsic Berry curvature effect and the Hall conductivity is proportional to the scalar spin chirality in the weak coupling limit of dirty conductors [88], [255]. The non-coplanar magnetic order with a geometrical correlation characterised as the scalar spin chirality. Asymmetric (skew) scattering of nonmagnetic chemical defect or single spin combined with spin-orbit interaction is treated as a small perturbation in the extrinsic mechanism, resulting in relatively small anomalous Hall angles, in contrast to the intrinsic mechanism. Skew scattering in ferromagnets, for example, occurs when an impurity's spin-orbit interaction (SOI) causes electrons to be scattered asymmetrically. However, when compared to the energy scale of the hybridization between the resonance state and the conduction electrons, this impact is less, so restricting the skew angle. The skew-scattering by multiple spins, on

the other hand, has no such restriction. [8,9,23], and occurs without SOI. Although a variety of mechanisms explored behind the AHE in 3D materials, the Hall angle $\frac{\sigma_{yx}}{\sigma_{xx}}$ is of the order of ~10^{-3}–10^{-2} as the AH conductivity σ_{xy} is small compared to the longitudinal conductivity σ_{xx} for most of the cases [256].

TIs can host a wide range of magnetic phases when doped with magnetic impurities, including ferromagnetic, paramagnetic, noncolinear, and spin glass phases, resulting from a variety of exchange interactions between the magnetic impurities and the surface, bulk states. These unique magnetic phases are required for originating AHE. Some previous approaches on doped TI focusing on magnetic and non-magnetic origin of the observed anomalous Hall effect are discussed in [257]–[260]. For instance, in pure ferromagnets, electrons deflected transversely by nonmagnetic impurities can cause AHE [261]. In a paramagnetic system MgZnO/ZnO heterostructures [262], the anomalous Hall effect arises from the skew scattering of electrons by localized paramagnetic centres. Skew-scattering produced AHE was achieved in magnetic cluster, spin cluster type of systems [90]. The anomalous Hall effect arising from the scalar spin chirality (noncoplanar spin structure) is established in many systems including ferromagnets as well as antiferromagnets [90], [263], [264]. In this mechanism, itinerant electrons are coupled to these noncoplanar magnetic orders and leads to nontrivial effects in the electron properties. A finite Berry phase is generated when electrons hop between magnetic atoms with a noncoplanar spin configuration that acts as an effective magnetic field. Surprisingly, AHE has been observed to appear even above the magnetic ordering temperature, indicating the thermal average of spin chirality, but the intrinsic AHE driven by Berry phase vanishes above ordering temperature[265]. Remarkably, in skyrmion systems, the origin of the large AHE above the ordering temperature is ascribed to a new type of skew-scattering via thermally excited

spin-clusters with scalar spin chirality [71], [264], [266], [267]. Later research revealed that vector spin chirality also contributes to the AHE [268], [269].

In the present investigation, we report spin chirality induced AHE in Dy doped $BiSbTe_3$ above Neel temperature. To the best of our knowledge, AHE above ordering temperature is hitherto lacking in Topological insulator family of compounds. The induced magnetism along with the frustrated exchange interaction evokes an AH signal. As the temperature enhances, thermal fluctuation continues the effect in the presence of intrinsic electronic topology (SOC). Motivated by the previous works on SSC produced AHE[88], [90], [266], [268], we found out $\sigma_{xy} \alpha \sigma_{xx}$ scaling and reached to a conclusion that this scattering is distinct from the impurity induced skew scattering process. The results imply rich physics related to the interplay of thermal fluctuation and magnetic scattering beyond the Berry-phase description.

5.2 Methods

5.2.1 Theoretical calculation We performed DFT calculation using Vienna ab initio simulation package (VASP). We adopted generalized gradient approximation (GGA) as exchange–correlation proposed by Perdew-Burke-Ernzerhof (PBE). All atoms of $Bi_{0.95}Sb_{0.95}Dy_{0.1}Te_3$ were fully relaxed with conjugate-gradient algorithm until a residual force is less than 0.01 eV $Å^{-1}$. A supercell of size 2 × 2 × 1 was generated (total 60 atoms out of which 12 Sb atoms, 12 Bi atoms, 36 Te atoms) for the calculation. 1 Sb and 1 Bi atom are substituted with 2 Dy atoms within the same quintuple. We followed the energy convergence limit up to 10^{-6} eV for all sets of calculations. The electronic calculations were performed using Γ-centred K-mesh of 2 × 2 × 1 with a plane-wave energy cutoff of 400 eV, spin orbit coupling (SOC) was included in the calculations. The Gaussian smearing method along with a smearing width equal to 0.10 eV was chosen for Brillouin zone integration.

We used experimental lattice parameters a = b = 4.3209(49) Å, and c = 30.5064(22) Å for the theoretical calculation of $Bi_{0.95}Sb_{0.95}Dy_{0.1}Te_3$. For DOS calculations NEDOS=1000 and NBANDS=400 was used.

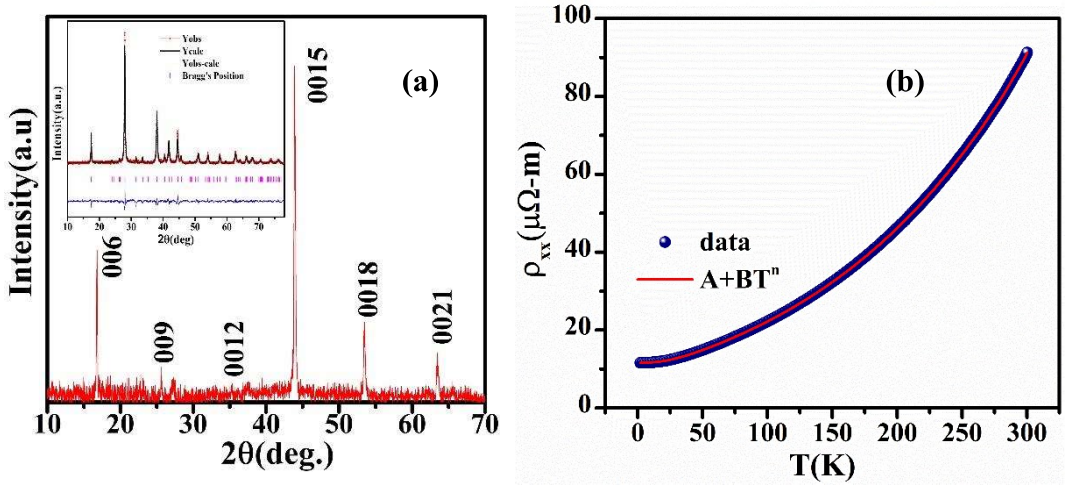

Figure 5.1 (a) Single crystal XRD and inset: powder XRD with Le-Bail refinement of $(BiSbDy)_2Te_3$, **(b)** Fitting of electron-electron interaction term $A+BT^n$ on the low temperature part of the resistivity data ρ_{xx}.

5.3 Results and Discussions

5.3.1 XRD Figure 5.1a and inset shows the single crystal and the powdered XRD pattern (left inset) of a $Bi_{0.95}Sb_{0.95}Dy_{0.1}Te_3$ single crystal. The XRD data collected on the powdered polycrystalline sample of Dy doped BST at room temperature were analysed by FULLPROF software. The crystallographic parameters found from the Le-Bail refinement are a=b= 4.320 Å, c= 30.506 Å. The XRD results unveil all the diffraction peaks corresponding to the (00l) family of rhombohedral planes, heralding that the sample was grown in the c direction and that the cleaved surface is an ab plane.

5.3.2 Zero field resistivity behaviour The metallic character of the sample is demonstrated by the temperature dependent resistivity (ρ_{xx}) behaviour shown in the Figure 5.1b. The resistivity values are at 2K and 300K are 1510.04 and 11879.66 μΩ-m respectively

rendering a RRR value $\frac{\rho_{xx}(300K)}{\rho_{xx}(2K)}$ =7.87. RRR has a value that is compatible with a number of topological materials [270]. Throughout the measured temperature range, the temperature evolution of the resistivity ρ_{xx} reveals metallic character for zero magnetic field i.e., ρ_{xx} decreases monotonically from room temperature.

5.3.3 Field effect on longitudinal resistivity The derivative of ρ_{xx} data (Figure 5.2a) exhibits a kink around 44.2 K and it is indicated by T_m. The low temperature resistivity data can be fitted for with a ρ_{xx} (T) = A + BT^n-type relation for n ~ 2, where A and B are constants. A perfect fit to the value n = 2 manifested pure electronic correlation-dominated scattering mechanism. The resistivity is sharply increasing with temperature and there is no sign of saturation from Figure 5.2a. The resistivity pattern is similar to [271], [272]. In a magnetic field perpendicular to the current direction,

the longitudinal (ρ_{xx}) and transverse resistivity (ρ_{xy}) was measured. The MR ratio (%) has been defined as $\left[\frac{\rho_{xx}(B)-\rho_{xx}(0)}{\rho_{xx}(0)} \times 100\%\right]$, where ρ_{xx}(B) is the resistivity under non-zero applied magnetic field (B) normal to the 'ab' plane and ρ_{xx} (0) is the resistivity at B = 0. Figure 5.3a shows the results of magnetoresistance (MR) measurements at various temperatures. Down to low temperatures and high magnetic fields, we were able to produce a quadratic, non-saturated positive MR. At 2 K and 7 T, the observed MR value is as high as 50 percent. The MR% decreases to 24.14% at 100K. The MR's field dependency is nearly quadratic, and a power law MR = a + bB^c with c = 1.92 can be fitted. As shown in Figure 5.3b, employing Kohler's rule

$$\boldsymbol{MR = \alpha\left(\frac{B}{\rho_0}\right)^m} \qquad \textbf{(5.1)}$$

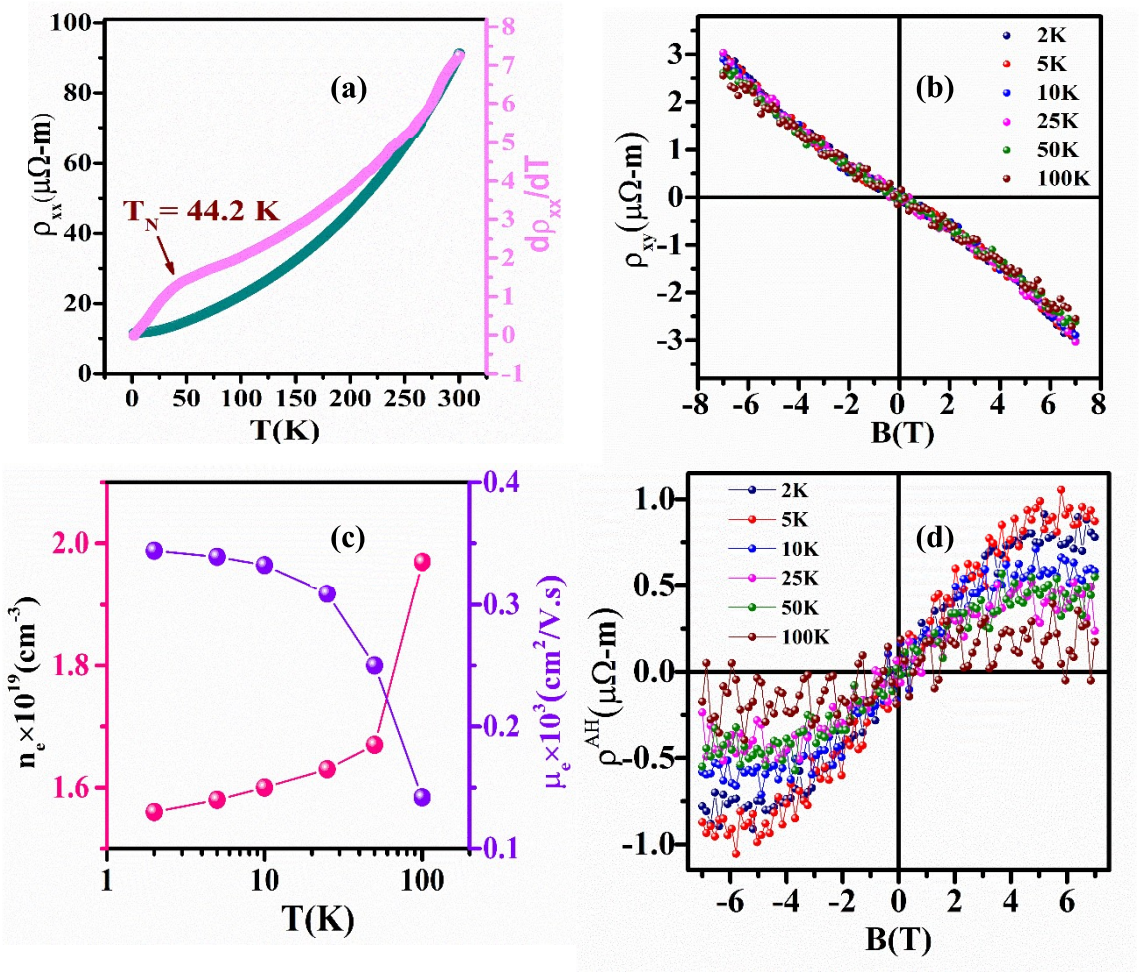

Figure 5.2 (a) Resistivity evolution with temperature in the range 2-300K(pink), the derivative of ρxx data exhibits a jump at 44.2K (green), **(b)** Hall data as a function of field at various temperatures ranging from 2-100K, **(c)** the extracted carrier density (ne) and mobility (μe) as a function of temperature, **(d)** The anomalous Hall part after extracting the linear part from the total Hall data.

with $\alpha = 3.35 \times 10^{-5}$ $(\Omega\ m/T)^{1.6}$ and m = 1.6. Multiple MR curves at various temperatures can be scaled to a single curve. This demonstrates that the current system's transport feature is due to a single type of charge carrier.

5.3.4 Hall effect To shed light on the transport behaviour, we carried out Hall resistivity ρ_{xy} measurements as function of B at different temperatures ranging from 2–100 K. The observed Hall resistivity ρ_{yx} is displayed as a function of magnetic field in Figure 5.2b. The negative slope of ρ_{yx} data over the whole temperature and field range signifies n-type nature

of the charge carrier and could be explained by Te vacancies and anti-site disorders [273]. The carrier concentration is calculated using the formula $n= 1/(R_H \times e)$, and the carrier mobility is calculated using the relation $\mu= 1/(\rho_{xx}|n|e)$, where e is the electron charge and ρ_{xx} is the electrical resistivity at zero magnetic field. The Hall data deduces nonlinear behaviour over the whole range and the nonlinearity decreases with increasing temperature. Importantly, the nonlinear Hall data emerges two possibilities- one is multiband transport i.e electron hole joint transport and another one is the anomalous Hall effect. The nonlinearity appears at low fields and low temperatures, but it fades with rising temperature and about to vanish above 100 K. In the present observation, Kohler's plot has already ensured single charge carrier transport. The carrier concentration (n_e) and carrier mobility (μ_e) were calculated from the slope of Hall data extracted at higher magnetic field region. The evolution of n_e and μ_e with respect to temperature is depicted in Figure 5.2c. The value of n_e at 2K is 9.13×10^{17} and increases to 1.15×10^{18} at 100K whereas the mobility decreases from 45.31cm^2/Vs at 100K to 18.69 cm^2/Vs at 2K. The AHE is one of the most important magnetic transport features, in which the combination of magnetism and spin-orbit coupling produces a transverse voltage perpendicular to the applied current and the magnetization. The electron density is comparatively lower than the other reports but similar to the case of diluted carriers in EuAs [265].

Extrinsic contributions from impurity scattering of charge carriers and intrinsic contributions from the Berry curvature of the electronic structure can both contribute to the AHE. Side-jump and skew scattering effects account for the majority of the extrinsic contribution, and by integrating the Berry curvature throughout the entire Brillouin zone, the intrinsic contribution of the AHE in a material is estimated [274]–[276]. The Hall resistivity can be written as $\rho_{xy} = \rho^0+\rho^{AH}$, where ρ^0 is ordinary Hall contribution ($\rho^0= R_OB$, where, R_O is the ordinary Hall coefficient, B is the magnetic field) and ρ^{AH} is the AHE

contribution, which comes from the magnetization of the material ($\rho^{AH} = R_{AH}M$, where R_{AH} is anomalous Hall (AH) coefficient, and M is magnetization of material).

We subtracted the ordinary Hall contribution from the measured Hall resistivity to get the AH contribution. As evinced from the magnetic M-T data, the magnetization tends to saturates above 4T, we consider that that the Hall data is independent of M above 4.5T. Similar results were observed in [277]. As indicated in the Figure 5.2d, the extracted AH part is positive. It is also evident from the Figure 5.2d that the anomalous part decreasing as the temperature increases from 2K to 100K and fade away over 100K.

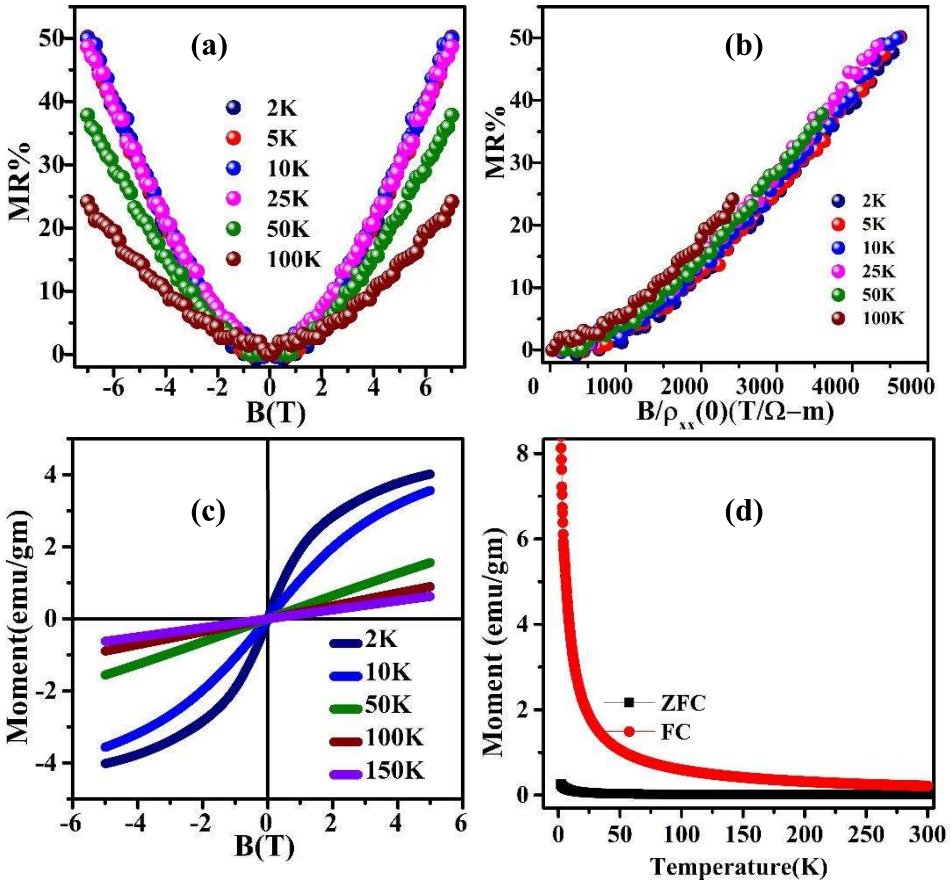

Figure 5.3 (a) MR% data with field at various temperatures 2K, 5K, 10K,25K, 50K,100K, **(b)** The fitting of MR% data with the Kohler's scaling $B/\rho_{xx}(0)$ scaling, **(c)** The variation of magnetization with field at various temperatures 2K,10K,50K,100K,150K, **(d)** The magnetization evolution with temperatures in ZFC and FC cycle.

To elucidate the mechanism behind AHE, one can extract the parameter β from scaling behavior of ρ^{A}_{xy} using the relation $\rho^{A}_{xy} \propto \rho_{xx}^{\beta}$ [278], where β= 1 assigned for skew scattering and β=2 signifies the contribution of intrinsic Berry curvature and extrinsic side jump effect. The longitudinal conductivity (σ_{xx}) and the Hall conductivity (σ^{A}_{xy}) were calculated using following relation-

$$\sigma_{xx} = \frac{\rho_{xx}\,(B=0)}{\rho_{xx}^{2}\,(B=0) + \rho_{xy}^{2}} \quad \text{and} \tag{5.2}$$

$$\sigma_{xy}^{A} = \frac{\rho^{A}_{yx}}{\rho_{xx}^{2}\,(B=0) + (\rho^{A}_{yx})^{2}} \tag{5.3}$$

Here, ρ_{xx} and ρ_{yx} are the longitudinal and Hall resistivity, respectively. For the calculation of σ_{xx} plotted in Figure 5.4c, we have used the longitudinal conductivity, where field dependent ρ_{xx} and ρ_{xy} has been taken into consideration

$$\sigma_{xx} = \frac{\rho_{xx}}{\rho_{xx}^{2} + \rho_{xy}^{2}} \tag{5.4}$$

The perturbatively tiny SOC compared to the electron bandwidth results in a small Hall angle in conventional skew-scattering (due to chemical defect or single spin) in the range of 0.1–1%. In addition, σ_{xy} should be monotonously increased to lower temperature with higher σ_{xx}. In the present system the Hall angle lies 22 (2K) to 9.5% (100K) unlike the conventional skew scattering. Again, the longitudinal conductivity σ_{xx} for the present case is $<10^{3}$ $(\text{ohm-cm})^{-1}$ which lies in dirty regime. For the case of intrinsic scattering, the Hall conductivity ranges ($10^{3} < \sigma_{xx} < 10^{5}$ $(\text{ohm-cm})^{-1}$), additionally it requires σ_{xy} to vary quadratically with σ_{xx}. In the previous studies based on BST compounds like Cr doped $BiSbTe_3$, where $\sigma_{xy} \alpha \sigma_{xx}^{\alpha}$ with $\alpha \sim 1.55$, the AHE was explained by variable range hopping (VRH) mechanism[257]. In a magnetic/non-magnetic topological insulator heterostructures, $Cr_x(Bi_{1-y}Sby)_{2-x}Te_3/(Bi_{1-y}Sby)_2Te_3$, the origin of the AHE was the reason

for skyrmions [279] . Here, in the current investigation, we can assume "spin cluster" mechanism previously discussed by [87], where a triangular spin cluster or tiled clusters act like a "compound magnetic scattering center". When an external field is applied, the distortion of the local order results in a net magnetization and magnetic fluctuations act as scattering centers generating an enhanced skew scattering potential [87]. But the values of σ_{xy} and σ_{xy} are not that large as discussed in "enhanced" case. However, the anomalous Hall angle (AHA) is quite large~18% in our system. In that sense, the skew-scattering in the present case differs from the normal skew-scattering caused by nonmagnetic chemical defects or single-spin impurities [71], [254], [280], [281], despite the fact that they have a comparable linear (σ_{xy} /σ_{xx}) scaling relation. Importantly, while the intrinsic AHE based on the Berry phase fades above ordering temperature, spin chirality induced AHE can appear even above the magnetic ordering.

A combination of induced magnetic doping and the spin frustration grant the present system to achieve AHE. As we have already seen that the frustration among the exchange interactions in the spin-glass system leads to noncollinear and noncoplanar spin configurations[250]. At the same time, this AHE appear above the magnetic ordering temperature, indicating the thermal average of spin chirality. Again, at a finite temperature around or above the magnetic transition temperature, magnetic scattering leads to skew scattering and it is proportional to thermal average of the scalar spin chirality[90]. The skew scattering means the asymmetric scattering between the impurities (or spins) and charge carriers in the presence of SOC. Thermal or magnetic fluctuation can also act as a scattering centre. Below transition temperature the skew scattering by spin clusters or tilted cluster is not possible here as this causes very large conductivity like[86], [265]. So, this is not the case of enhance skew scattering, rather at finite temperature above T_N, the frozen clusters get melted to single spins causes further scattering effects under thermal fluctuations. This

matches with the observed bifurcation of the ZFC-FC data. We speculate that these atomic spins participate in the skew scattering mechanism above T_N.

In the present investigation Hall angle (order of ~22%) is large compared to the conventional limits of AHE of intrinsic and extrinsic origins, respectively [265], [266]. But the Hall conductivity is less, compared to the enhanced skew scattering cases, in the range of ~183.13-42.63 $(\Omega\text{-cm})^{-1}$ and survives above the ordering temperature. So, it may be possible that the thermal fluctuations of the spins are responsible behind this AHE up to 100K. At low temperature it is introduced magnetism along with SOC causing the AHE. Additionally, the spin cluster present is occurring the additional skew scattering phenomena. The contour map of σ_{xy} is demonstrated with the magnetic phase diagram in Fig. 8b to endow an overview of this Hall response in the B–T plane. The Hall response is significantly increased at low temperatures below 40 K, close to the AFM-PM boundary. Figure 5.4a interprets various mechanisms that might lead to skew scattering AHEs.

5.3.5 Magnetic behaviour Magnetic measurements were performed to investigate the origin of AHE and observed striking behaviour (T_m) in the derivative of the resistivity data. Figure 5.3c, d shows M-H and the temperature-dependent magnetic susceptibility (χ) data measured in a zero-field cooled (ZFC) and field cooled (FC) condition with a magnetic field of 0.1T. Magnetization as a function of magnetic field (M–H) revealing non saturating magnetization behaviour with zero hysteresis, supporting the AFM ordering below 50K. The sharp jump in the temperature dependent ($d\rho_{xx}/dT$) curve at ~44.2 K was identified as transition temperature T_N. The M(H) curve is clearly linear at temperatures above 100 K, which is consistent with Curie-Weiss paramagnetic behaviour. The observed M-H curve continues to show paramagnetic behaviour up to room temperature. To estimate the effective paramagnetic moment (μ_{eff}) and Curie-Weiss temperature (θ_{cw}), we fitted the

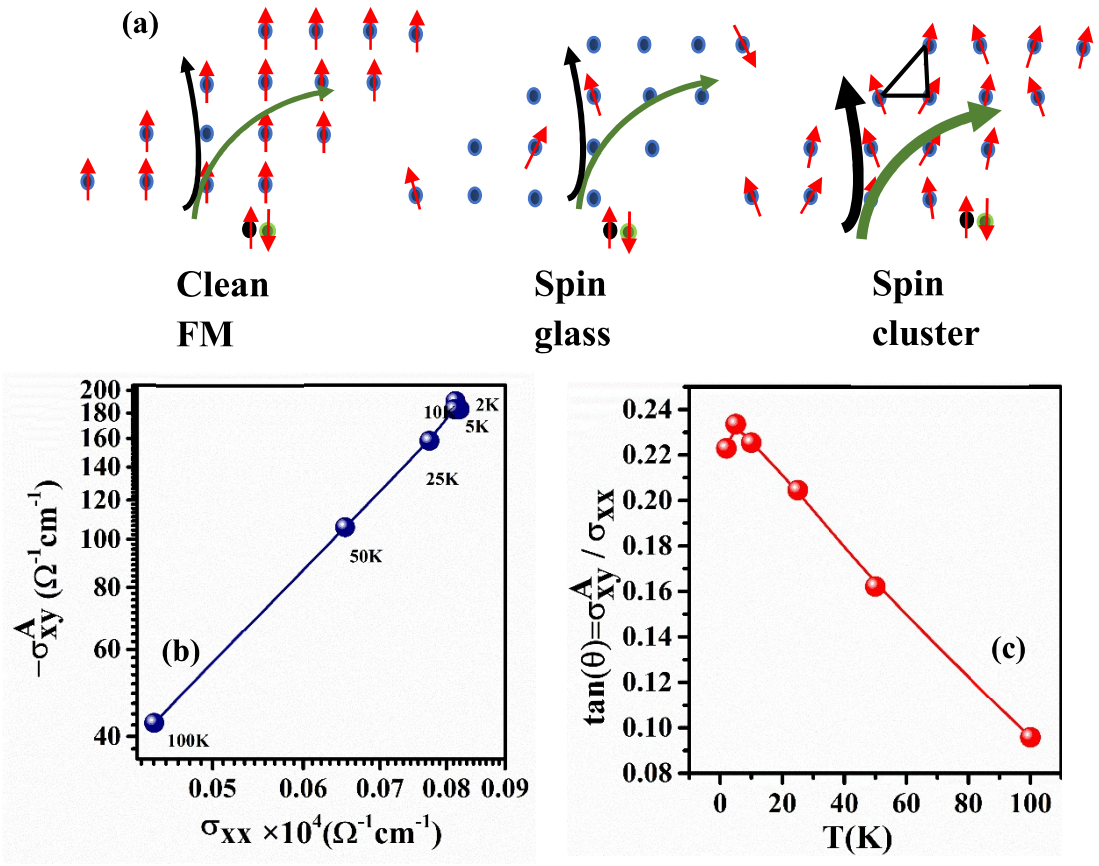

Figure 5.4 (a) The schematic of the different skew scattering mechanism in a clean FM, spin glass and cluster glass systems, **(b)** The anomalous Hall conductivity as a function of longitudinal conductivity, $\sigma_{xy}\alpha\sigma_{xx}$ scaling showing skew scattering behaviour, **(c)** the anomalous Hall angle as a function of temperature.

effective paramagnetic moment (μ_{eff}) and Curie-Weiss temperature (θ_{cw}), we fitted the inverse susceptibility χ^{-1} vs T data by Curie Weiss (CW) law:

$$\frac{1}{\chi} = \frac{3K_B}{\mu^2_{eff}}(T - \theta_{CW}) \qquad (5.5)$$

in the paramagnetic region [where, K_B=Boltzman constant]. The fitting yield θ_{cw} = -9.69 K and μ_{eff} ~10.62 μ_B. The presence of the dominant antiferromagnetic interactions between the Dy-local moments is indicated by the negative value of θ_{cw}. The large temperature difference between θ_{cw} and T_N reflects presence of system's spin frustration. A spin-

freezing characteristic is observed with subsequent cooling. The χ_{dc} (T) shows a divergence behaviour below 250K between ZFC and FC cycle. A hallmark feature of a spin-glass ordering is that the position of AC susceptibility maxima rises with increasing excitation frequency. Figure 5.5 (a), (b) illustrates the temperature dependence of the real (χ'_{ac}) and imaginary (χ''_{ac}) parts of the ac magnetic susceptibility of the present system measured in an excitation field of H_{ac}=3 Oe at various frequencies (f). Both the components of χ_{ac} reveals distinct anomalies, the amplitude and peak position of which depend on the frequency of the applied ac magnetic field. The real part of the χ'_{ac} (T) displays a valley at ~10 K, which shifts to higher temperatures with increasing the frequency of the applied ac fields. This trend is quite similar in the imaginary part of the AC susceptibility χ''_{ac} (T). A standard measure for comparing the frequency dependence of T_f in different spin-glass systems is the relative shift in freezing temperature per decade of frequency-

$$\delta T_f = \frac{\Delta T_f}{T_f \Delta(log_{10} f)} \tag{5.6}$$

For this material we found δT_f=0.019 (Mydosh parameter [282]) which is intermediate between the noninteracting ideal superparamagnetic systems and canonical spin-glass systems[282]. This value is comparable to other cluster glass systems [283]. Moreover, the spin dynamics in a glassy state gets slowed down below the critical temperatures T_f which can be investigated using the dynamic scaling law[282]-

$$f = f_0 \left(\frac{T_f - T_{SG}}{T_{SG}}\right)^{z\upsilon} \tag{5.7}$$

f is related to the frequency for which χ'(T) reaching a maximum at T=T_f, T_{SG} is the

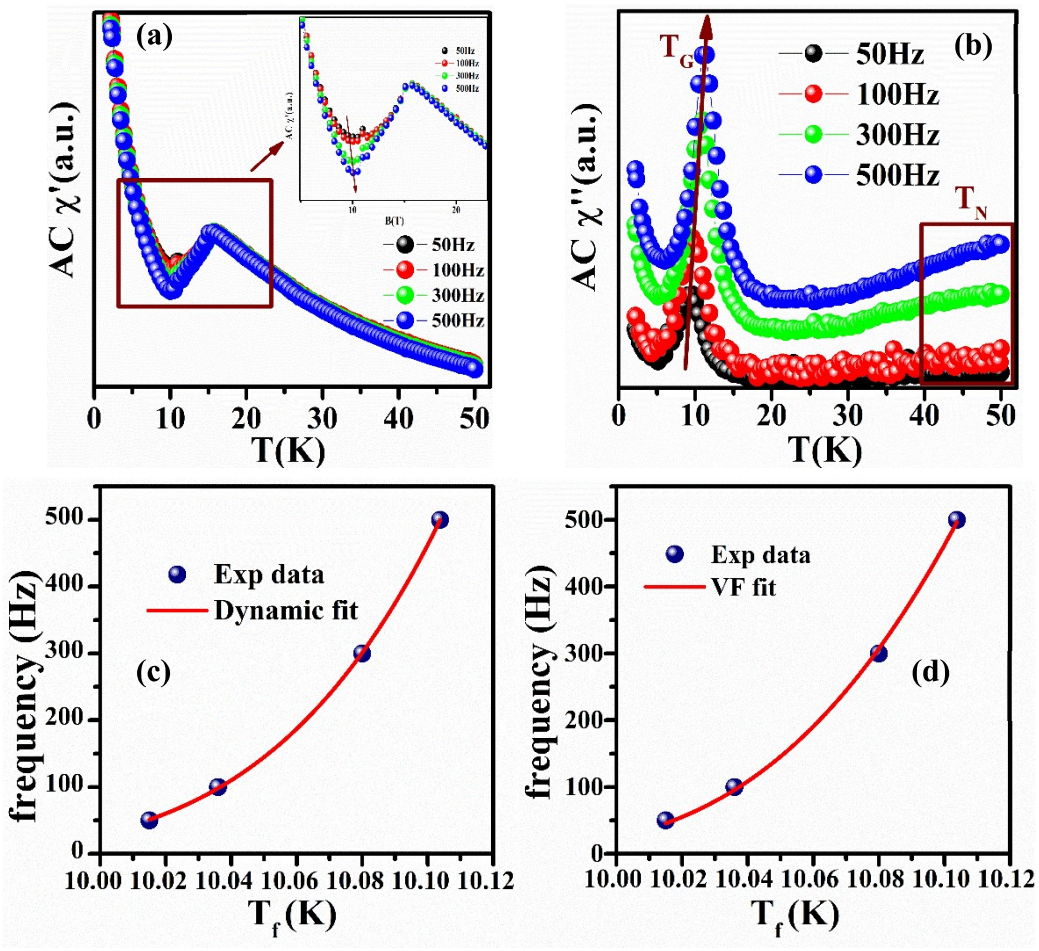

Figure 5.5 (a) The AC susceptibility **(a)** real part and **(b)** imaginary part as a function of temperature at different frequencies, **(c)** The anomalous and Hall conductivity as a function of temperature, **(c)** frequency vs T_f plot, the best fit shows Dynamic fitting, **(d)** frequency vs T_f plot, the red line shows VF fitting.

equivalent spin-glass freezing temperature as f → 0 Hz and H_{DC} → 0 Oe, zν is the dynamic critical exponent, f_0 is related to the characteristic relaxation time ($\tau_0=1/f_0$) of single spin flip. The best fitting of the f vs T_f curve (Figure 5.5c) gives zν~4.49, T_{SG}=9.88±0.26. The value of zν is in line with the SG/CG systems (zν ~4-12). τ_0 value obtained from the fitting $10^{-10}s$.

The equation (5.7) can be rearranged in the following way to assess the accuracy of the fitted parameters-

$$ln(\tau) = \ln(\tau_0) - z\upsilon\, ln(t) \quad (5.8)$$

where $t = (T_f - T_{SG})/T_{SG}$. We used the value of T_{SG}= 9.89K for fitting of ln(τ) vs ln(t) curve. We got the value of T_{SG} by extrapolating f to 0 in T_f vs f plot. The slope and intercept yields zυ=4.288 and $\tau_0 = 1.56\times10^{-10}$s. Furthermore, to mention that the value of τ is comparatively larger than the canonical SG ($\tau=10^{-12}$) suggesting strongly interacting clusters rather than individual spins. Moreover, T_f deviates from the Arrhenius law[282], indicating the presence of interacting clusters.

$$f = f_0\, exp\left(\frac{-E_A}{K_B T_f}\right) \quad (5.9)$$

where k_B is the Boltzmann constant, f_0 is the characteristic attempt frequency, and Ea is the average thermal activation energy. The ln(f) vs $1/T_f$ picture Figure 5.6b, however, shows that there is a large divergence from the expected linear behaviour at low frequencies, showing that the dynamics are not related with single-spin flips, but rather reflect a cooperative nature of the freezing-in process. The fitting yields unphysical values of E_A/K_B and f_0. To better understand the interaction strength between magnetic entities, Vogel-Fulcher law was employed[282]-

$$f = f_0\, exp\left(\frac{-E_A}{K_B(T_f - T_0)}\right) \quad (6.0)$$

where T_0 represents interaction strength between dynamic entities and E_A is the activation energy. The best fit Figure 5.5d yields E_A=0.128 meV(1.49K), T_0= 9.81 K. The τ_0 value obtained from the VF fitting $10^{-6}s$ is orders of magnitude larger than the spin-flip time of atomic magnetic moments (~10^{-13} s) and SG systems(~$10^{-11} - 10^{-13}$s) but comparable to the typical CG systems (~$10^{-6} - 10^{-10}$s). This indicates towards spin clusters rather than atomic spins. The T_{SG} and τ_0 obtained using power law are comparable to T_0 and τ_0 for the VF law. A nonzero value of T_0 arises from the interaction between the spins and

indicates the formation of clusters [283]. The value of activation energy 0.128meV is quite comparable to other cluster glass category[284].

In the present investigations, $T_0 > E_a/k_B$ suggesting a strong coupling between the magnetic entities whereas $T_0 < E_a/k_B$ indicates a weak coupling according to the VF model [285]. The above equation can be rewriting as-

$$T_f = exp\left(\frac{E_A/K_B}{ln(f_0/f)}\right) + T_0 \quad (6.1)$$

we fixed the value of $f_0 = 1.236 \times 10^{-10}$ s. The best fitting Figure 5.6c of T_f vs $100/\ln(E_A/K_B)$ results T_0=9.35K and E_A/K_B=0.127K. To verify those parameters obtained so far, we rearranged the equation-

$$ln\, f = ln\, f_0 - \left(\frac{E_A/K_B}{T_f - T_0}\right) \quad (6.2)$$

This would allow us to calculate Ea/k_B and τ_0 using the slope and intercept of the ln(f) vs $1/(T_f\ T_0)$ plot Figure 5.6d, respectively. The fitting gives τ_0 of the order of 10^{-6} and E_A/K_B=0.7786K or $E_A = 0.0777K_BT_f$ from the peak temperature of χ'_{ac} (T). Furthermore, the fact that T_0 is so close to T_f indicates that the Ruderman-Kittel-Kasuya-Yosida (RKKY) interaction in our compound is relatively strong. The Tholence criterion[286]-

$$\delta T_{Th} = \left(\frac{T_f - T_0}{T_f}\right) = 0.066 \quad (6.3)$$

we used for T_f = 10.015 K (for f = 50 Hz) and T_0 = 9.35 K as obtained from previous analysis. This value of δT_{Th} is comparable to CuMn[286] (δT_{Th} =0.07) or $PrRhSn_3$[283] (δT_{Th} =0.076) type of spin-glass systems with dominant RKKY interactions.

In order to understand the electronic structure, we have performed bandstructure calculation (Figure 5.7b) using DFT software. The calculated band structure was plotted

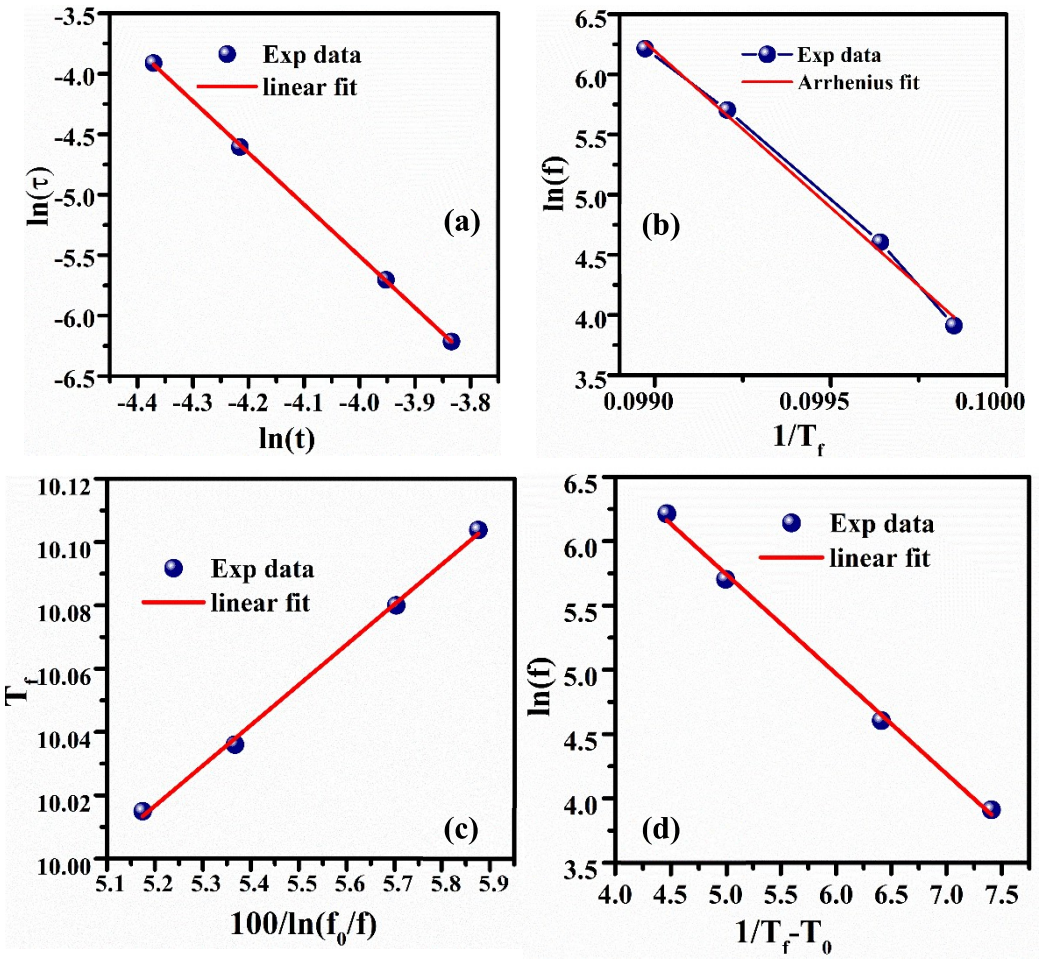

Figure 5.6 (a) The frequency dependence of freezing temperature plotted as a ln(τ) vs ln(t), where reduced temperature $t = (T_f - T_{SG})/T_{SG}$, the red line represents the linear fit to extract zυ and τ, **(b)** ln(ν) vs $1/T_f$, the red line denotes the Arrhenius fitting to extract the thermal activation energy E_A and characteristic attempt frequency f_0, **(c)** T_f vs $100/\ln(f_0/f)$, the solid line represents the linear fit to evaluate E_A and intercluster interaction strength T_0, **(d)** ln(ν) vs $1/(T_f - T_0)$, the red line denotes the linear fit to extract the thermal activation energy E_A and τ_0.

for momentum space in the direction of K–Γ–M of the Brillouin zone. The GGA+U functional was used to avoid the underestimation of the energy band gap. To incorporate the f-states electrons in the calculation we used U = 6.0 eV, as suggested in [287]. From the Figure 5.7b it is evident that the conduction band minimum crosses the Fermi energy level, which is in agreement with the measured n-type Hall data.

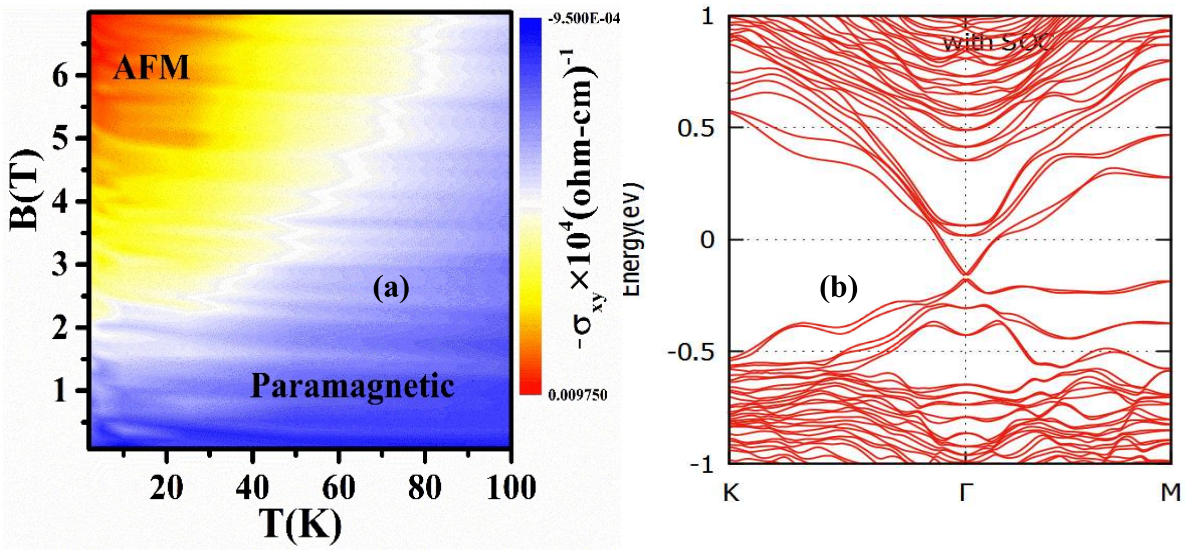

Figure 5.7 (a) Contour plot of σxy in the B–T space with the magnetic phase diagram consisting of the antiferromagnetic (AFM) and paramagnetic (PM) phases, (b) the bandstructure of Dy doped $BiSbTe_3$ system.

5.3.6 sdH oscillation The fast Fourier transformation (FFT) spectra of these M oscillations are shown in Figure 5.8a. A single peak may be found at frequency (F) 50.4 T, which corresponds with the results of Ref.[111], [288]. According to the Onsager relation $F = (\hbar/2\pi e)A_F$, the cross-sectional area of FS (AF) normal to B is calculated to be 0.48 nm^{-2}. These results are in line with [111], [288]. One can obtain Fermi momentum vector $k_F \sim 3.8$ $Å^{-1}$. Again, the Fermi velocity $v_F = \hbar k_F/m^* \sim 2.16 \times 10^6$ m/s, where we have used $m^* = 0.185m_0$ for N=6 LL[288], and Fermi energy $E_F = m*v_F^2 \sim 4.92$ eV. Figure 5.8b plots the LL fan diagram for the $F\alpha$ band, where M peaks and valleys are assigned as N-3/4 and N-1/4 (LL indices), respectively [289], and fall onto a straight line. A linear fitting of N vs $1/B$ gives an intercept of 0.26 and thus the Berry phase $\varphi_B = 2\pi(0.26 + \delta) = 0.52\pi$ [290]. Here, δ is the FS dimension-dependent correction to a phase shift, of which the value varies from 0 for 2D FS to +1/8 or −1/8 for a minimum or maximum cross section of 3D FS, respectively [291]. For the calculation we assumed $\delta = 0$, because of the 2D Fermi surface

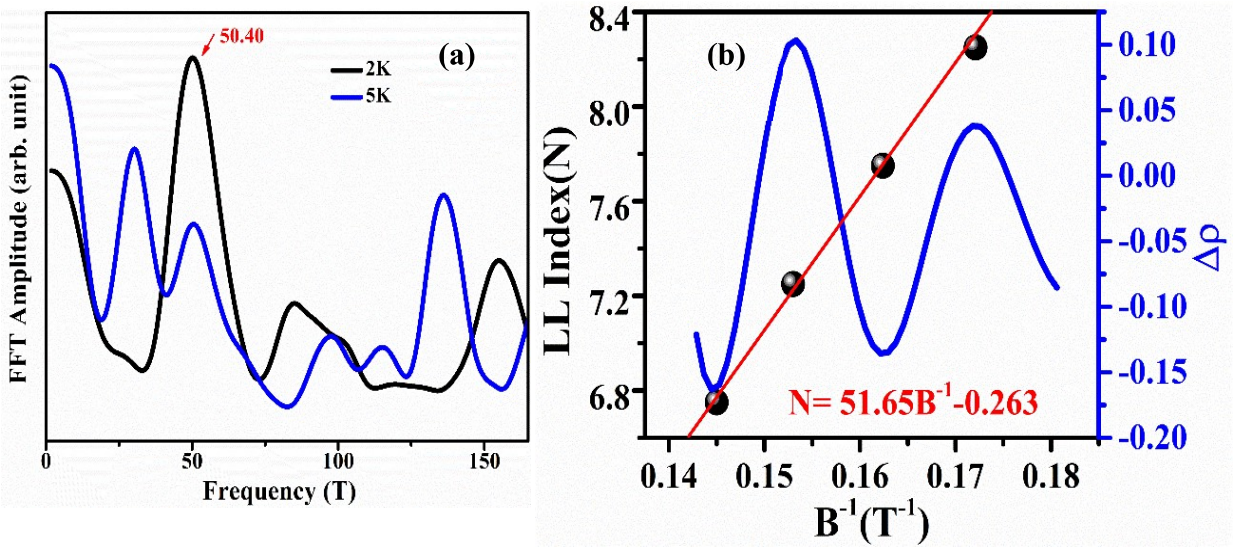

Figure 5.8 (a) FFT of the original resistivity ρ_{xx} vs 1/B data to extract the particular frequency of the oscillation, this particular frequency(50T) is proportional to the area of the Fermi, and **(b)** inverse FFT to obtain 50T frequency signal in time scale, red solid line shows Landau Fan diagram to extract the phase and frequency of the signal.

in $BiSbTe_3$ [292]. So, we can conclude that the Fermi surface topology does not change, the single frequency at F=50T also clarifies that the SdH oscillations in our sample might be attributed to the TI surface state. It is also obvious that the nonlinearity in the Hall data is not related to multiband charge transport rather coming from AH effect.

5.4 Conclusions

In summary, we have studied magnetic, transport and electronic properties of rare earth doped $BiSbTe_3$ system. The system exhibits AHE at a temperature far away from T_N, AFM spin fluctuations evolving on the frustrated lattice. The spin frustration is observed from the bifurcation of ZFC-FC data. The ac-susceptibility measurements demonstrate a shift in T_f with excitation frequency, indicating that the system is a frustrated one. Considering that the signal appears centered at the paramagnetic phase, skew scattering by individual spins with finite spin chirality is a possible origin of the observed AHE observed in the noncoplanar spin texture. Up to magnetic transition temperature it is the concomitant effect

of magnetism and frustrated lattice that realizes this extraordinary effect. Additionally, at finite temperature the thermal fluctuation of the spins providing the fuel to cause AHE to survive above T_N. The cluster glass state is confirmed by the slower dynamic of the spins and evaluated by Dynamic fitting. The presence of cluster formation was further assessed by departure of Arrhenius plot, and finally we concluded the intercluster interaction to be strong by VF fit. The nontriviality of the current material is proved by the π- Berry phase of Landau Fan diagram. Investigation of large AHE from the perspective of short-range spin correlation would pave the way for new electronic functions to be discovered.